



Construction of a rapid simulation design tool for thermal responses to laser-induced feature patterns

T. I. Zohdi¹

Received: 30 July 2017 / Accepted: 25 October 2017
© Springer-Verlag GmbH Germany, part of Springer Nature 2017

Abstract There are many emerging manufacturing processes whereby surface structures are processed by spatially laser patterning of an entire feature at a time, as opposed to rastering a small beam. It is important to ascertain and ideally control the induced thermal fields underneath the pattern. This paper develops a computational framework to rapidly evaluate the induced thermal fields due to application of a laser on the surface. The aggregate thermal fields are efficiently computed by superposing individual “beamlet” heat-kernel solutions, based on Green’s functions, to form complex surface patterns. The utility of the approach is that laser-process designers can efficiently compute the results of selecting various system parameters, such as spatially-variable laser intensity within a pattern. This allows one to rapidly compute system parameter studies needed in the manufacturing of new products. Included are:

- A computational framework to compute the time-transient thermal response from a spatio-temporally non-uniform laser beam in an arbitrary spatial pattern and
- An analysis of how the results can be used to track the evolution of the thermal gradients and their correlation to thermal stresses.

Three-dimensional examples are provided to illustrate the technique. The utility of the approach is that an analyst can efficiently ascertain a large number of laser-input scenarios without resorting to computationally-intensive numerical procedures, such as the Finite Element Method.

✉ T. I. Zohdi
zohdi@me.berkeley.edu

¹ Department of Mechanical Engineering, University of California, Berkeley, CA 94720-1740, USA

Keywords Laser · heat-transfer · manufacturing

1 Introduction

The dramatic increase in computational power for mathematical modeling and simulation opens the possibility that scientific computing can play a significant role in the analysis of many emerging complex manufacturing processes involving lasers. However, for this goal to be realized computational tools need to be developed which can allow engineers and scientists to quickly design and analyze new multistage manufacturing processes by testing hundreds, if not thousands, of scenarios. In many cases, these manufacturing processes may involve laser processing of the material in targeted regions, in order to process materials in ways that are very difficult or impossible with classical manufacturing methods. *Laser processing*, which utilizes high-intensity beams to heat the material to desired temperatures either to subsequently bond, soften, sinter, melt or ablate (Fig. 1), in a very targeted manner. Laser-based heating is quite attractive because of the degree of precision that it allows. Specifically, because of the monochromatic and collimated nature of lasers, they are an attractive, highly-controllable, way to process materials. The range of power of a typical industrial laser is relatively wide, ranging from approximately 100–100000 W, thus providing wide latitude in their use.

1.1 Objectives of this paper

One concern of manufacturers is the evolution of thermal response of a material and the subsequent thermal stresses, and possible defects generated by imprecisely controlled heat affected zones, brought on by miscalibration of the laser power needed. For example, due to the rise of one particular

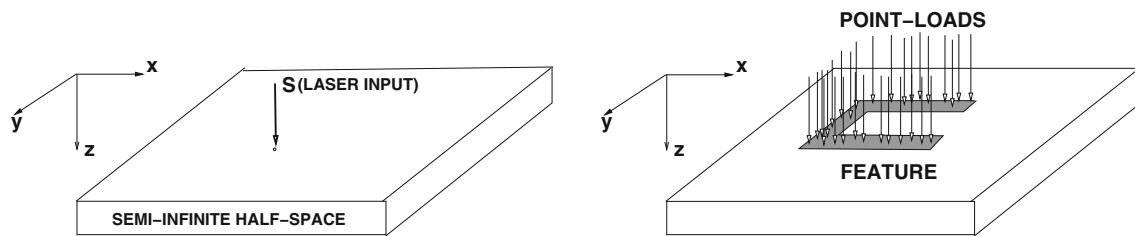


Fig. 1 Left: Fundamental building block, the point heat-load. Right: Building a “feature” from point heat-loads

branch of additive manufacturing, printed flexible electronics, involving sensitive substrates, it has become important to precisely understand how much laser-input is needed. For example, one possible remedy for this is to spatially “shape” the laser according to the geometry of the target zone. Thus, in order for *emerging manufacturing approaches to succeed, one must draw upon rigorous theory and computation to guide and simultaneously develop design rules for upscaling to industrial manufacturing levels. Commercial applications include sectors of aerospace, shipping, transportation, rail, automobile and medical and technology areas associated with engine parts, structural parts, mechanical or electrical parts, medical prosthetics, tooth implants. This motivates the present analysis.*

A general overall objective is to develop laser-based systems with adaptive cross-sectional beam shaping control to be used within advanced manufacturing processes. Laser processes where an entire feature is processed are often referred to as “flash processes”. In theory, these processes are advantageous since one can control the spatio-temporal distribution of the laser power over the target, as opposed to a small beam that rasters back and forth over the target zone. This control would also allow one to manage thermal stresses more effectively. However, such proposed processes are new, and some analysis and calibration is needed. In particular, it is important to ascertain and ideally control the induced thermal fields under a feature pattern. Accordingly, this paper develops a computational framework to *rapidly* evaluate the induced thermal fields due to multiple, simultaneous, surface inputs, which combine to form a “patterned laser”. The aggregate thermal fields are efficiently computed by superposing individual beamlet heat-kernels solutions, based on classical Green’s functions (fundamental solutions, Fig. 1), to form complex surface patterns. The utility of the approach is that process designers can efficiently compute the results of varying system parameters, such as spatio-temporally-variable laser intensity within a pattern as well as temporal variation. This allows one to *rapidly* compute system parameter studies needed in new product development, leaving more computationally-intensive “brute-force” coupled thermo-mechanical PDE discretization, based on Finite Element or Finite Difference methods towards the end of the system design phase.

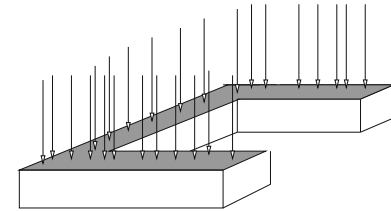


Fig. 2 An example to estimate the power needed to induce melting of a feature

Remark There are a large number of multi-step manufacturing processes that deposit material onto a surface in order to build a component, which are commonly referred to as “additive” (adding material) manufacturing methods.¹ In 2017, additive manufacturing was three billion dollar industry. In such fabrication processes it is important to ascertain the thermal gradients, and ultimately the thermal stresses. Applications are wide-ranging, for example, optical coatings and photonics (Nakanishi et al. [24]), MEMS applications (Fuller et al. [12] and Samarasinghe et al. [28]) and even biomedical devices (Ahmad et al. [1]). There are a wide variety of additive-like processes and we refer the reader to Gamota et al. [13], Sirringhaus et al. [32], Wang et al. [33], Huang et al. [15], Choi et al. [3–6], Demko et al. [8, 9], Fathi et al. [11], Martin [22, 23] and Zohdi [41–43] for details. These types are similar to spray coatings, and we refer the reader to the extensive works of Sevostianov and Kachanov [29–31], Nakamura and coworkers: Dwivedi et al. [10], Liu et al. [20, 21], Nakamura and Liu [25], Nakamura et al. [26] and Qian et al. [27] and to Martin [22, 23] for the state of the art in deposition technologies. Oftentimes, the objective is to produce multilayer coatings on curved surfaces (see, for example Grekov and Kostyrko [14]). The interested reader is referred to the recent overview article by Huang et al. [16] on additive manufacturing.

1.2 Qualitative a priori power-input/temperature estimates

In order to *estimate* the energy input needed to induce a desired temperature, consider the total mass in the fea-

¹ This is in contrast to (classical) “subtractive” processes which subtract material (for example using milling) to fabricate a component.

ture/process zone, such as the C-shaped domain in Fig. 2, denoted as m . In order to simplify the analysis, we employ a lumped mass model for the feature shown in Fig. 2 (the control volume). We remark that the validity of using a lumped thermal model, i.e. ignoring temperature gradients and assuming a uniform temperature within a feature, dictated by the magnitude of the Biot number. A small Biot number (significantly less than unity) would indicate that such an approximation is reasonable, which indicates that a uniform temperature distribution is appropriate, since the feature is considered small. *It is not in most cases, but the solution still provides qualitatively useful information.* The first law of thermodynamics reads as, assuming all energy is trapped in the feature domain and that it is uniform:

$$mC\dot{\theta} = S, \quad (1)$$

where θ is the temperature in the feature, $m = \rho V_f$, V_f is the volume of the feature, C is the heat capacity and S is the laser input (Watts). The solution to this differential equation is

$$\theta(t) = \frac{St}{\rho V_f C}. \quad (2)$$

Setting $\theta(t) = \theta_{melt}$ yields a simple relationship that correlates the power input, feature size, heat capacity desired temperature and processing time. This relationship ignores conductive losses and phase-transformations (latent heats). One can invert this to yield, for a desired temperature at a desired time $\theta^* \stackrel{\text{def}}{=} \theta(t = t^*)$:

$$t^* = \frac{\theta^* \rho V_f C}{S}. \quad (3)$$

One can improve this estimate by including conductive losses to the surroundings, given by an overall energy balance (First Law of Thermodynamics) is

$$\dot{\theta} = \frac{IK A_c}{mCh}(\theta_s - \theta) + \frac{S}{mC}, \quad (4)$$

where A_c is the area surrounding the feature where conduction takes place, θ_s is the average temperature surrounding the feature and h is a length-scale for conduction (essentially a small boundary layer thickness). For simple cases, this model can be solved analytically, for example for a constant laser input

$$\theta(t) = \theta_s + \frac{Sh}{IK A_c} \left(1 - e^{-\frac{IK A_c t}{mCh}} \right). \quad (5)$$

The relation above is important since it provides a qualitative connection between the temperature, to the laser input, conductivity, contact area and time. For example, if one set

the desired temperature at a desired time to be $\theta(t^*) = \theta^*$ one can solve for the laser input needed

$$S^* = \frac{(\theta^* - \theta_s) IK A_c}{h \left(1 - e^{-\frac{IK A_c t^*}{mCh}} \right)}. \quad (6)$$

We have the following observations:

- The rise time for the temperature is dictated by the ratio of conduction to heat capacity, $\frac{IK A_c}{mCh}$.
- At steady-state, $e^{-\frac{IK A_c t}{mCh}} \rightarrow 0$, and

$$\theta(t) = \theta_s + \frac{Sh}{IK A_c}, \quad (7)$$

which indicates that the ratio of S to $\frac{K}{h}$ dictates the steady state temperature.

- For a highly conductive surrounding: $IK \rightarrow \infty$, $\theta(t) = \theta_s$, where the conductive losses are instantaneous. This will draw heat away from the targeted zone.
- For a poorly conductive surrounding: $IK \rightarrow 0$, $\theta(t) = \theta_s + \frac{St}{mC}$, where the conductive losses are zero. This will trap (maximize) heat in the targeted zone.

Importantly, we can qualitatively describe the processing time by inverting the derived relationship:

$$t^* = -\frac{mCh}{IK A_c} \ln \left(1 - (\theta^* - \theta_s) \frac{IK A_c}{Sh} \right). \quad (8)$$

These expressions should be considered as providing the shortest possible times to process the target, and should be used only as qualitative guide and a starting point for numerical simulations. Because of the feature geometry, non-uniform thermal gradients, etc, the actual time is typically much greater, thus motivating the more advanced procedure outlined next.

Remark The ratio of the contributing terms are (leaving the dimensions of the target and the laser-power as variables):

$$\begin{aligned} \frac{\text{LASER}}{\text{CONDUCTION}} &= \frac{hS}{IK(\theta_s - \theta)A_c} \\ &\approx \frac{\mathcal{O}(10^3 h)}{\mathcal{O}(10^1 10^3 A_c)} = \frac{h}{10A_c}. \end{aligned} \quad (9)$$

Thus, depending on the length scale at which conduction gradients take place and the dimensions of the feature, the laser or conduction can dominate. Since $A_c \propto h^2$,

$$\frac{\text{LASER}}{\text{CONDUCTION}} = \frac{1}{10h}. \quad (10)$$

Thus, for small features, $h \approx 0.001$, the laser input dominates conduction.

2 Laser-induced thermal field: superposed-heat kernel approach

Our basic approach is to represent the contribution of the laser as a collection of point-zoloads on an infinite half space. Afterwards, we sum all of the contributions to obtain the total induced thermal field in the target. The most basic type of conduction model, which we will use, is the classical Fourier-type:

$$\mathbf{q} = -\mathbf{IK} \cdot \nabla \theta, \quad (11)$$

where θ is the temperature, \mathbf{q} is the conductive heat flux, \mathbf{IK} is the thermal conductivity (assumed isotropic). A balance of power, momentarily ignoring the effects of deformation and stress reads as

$$\rho \dot{w} = \rho C \frac{\partial \theta}{\partial t} = -\nabla \cdot \mathbf{q} + \mathcal{S}^{vol}, \quad (12)$$

where ρ is the mass density, $w = C(\theta - \theta_o)$ is the stored thermal energy, θ_o is a reference temperature, C is the heat capacity and \mathcal{S}^{vol} represents other sources (Watts per unit volume), such as **laser energy input**.

2.1 Point-source solutions

The temperature increase due to a point thermal load on a half-space is²

$$\Delta\theta(x_1, x_2, x_3, t) = \frac{S}{4\rho C(\pi D)^{3/2}} \int_{\tau=0}^t \frac{e^{-\frac{R^2}{4D(t-\tau)}}}{(t-\tau)^{3/2}} d\tau, \quad (13)$$

where $D = \frac{\mathbf{IK}}{\rho C}$ is the so-called thermal diffusivity, S is the heat input rate in Watts and $R \stackrel{\text{def}}{=} \sqrt{(x_1^* - x_1)^2 + (x_2^* - x_2)^2 + (x_3^* - x_3)^2}$ is the distance away from the point of application \mathbf{x}^* . This integral equation can be solved by first making a change of variables:

$$\beta = \frac{R}{(4D(t-\tau))^{1/2}} \Rightarrow d\beta = \frac{R}{4(D(t-\tau))^{3/2}} d\tau. \quad (14)$$

Thus,

$$\Delta\theta(x_1, x_2, x_3, t) = \frac{S}{\rho C D^{1/2} \pi^{3/2} R} \int_{\beta=\frac{R}{2(Dt)^{1/2}}}^{\infty} e^{-\beta^2} d\beta. \quad (15)$$

² The top is assumed insulated except where the load is present. See classical works of Jaeger [17] and Carslaw and Jaeger [2] for a complete, rigorous, derivation, and reviews in Kennedy [19] and Kachanov et al. [18]. The solution is obtaining by superposing a series of instantaneous thermal pulses and adding/integrating the solutions to represent a continuous source.

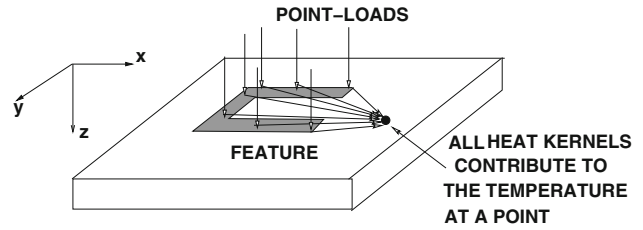


Fig. 3 All the point heat-loads contribute to the temperature at a sampling point

Since the integral can be rewritten using the complementary error function:

$$\text{erfc}\left(\frac{R}{2(Dt)^{1/2}}\right) \stackrel{\text{def}}{=} \frac{2}{\pi^{1/2}} \int_{\beta=\frac{R}{2(Dt)^{1/2}}}^{\infty} e^{-\beta^2} d\beta, \quad (16)$$

the solution becomes

$$\Delta\theta(x_1, x_2, x_3, t) = \frac{S}{2\rho C D \pi R} \text{erfc}\left(\frac{R}{2(Dt)^{1/2}}\right). \quad (17)$$

When $t \rightarrow \infty$, $\beta \rightarrow 0$, $\text{erfc}(0) \rightarrow 1$, and the steady-state solution becomes

$$\Delta\theta(x_1, x_2, x_3, t = \infty) = \frac{S}{2\rho C D \pi R}. \quad (18)$$

2.2 Construction of time-varying spatial patterns

The point-load formalism, namely starting with individual incremental point-load pulses, then integrating them is a quite useful in two ways: (1) Construction of time-varying loading solutions and (2) Construction of spatial patterns (Fig. 3).

2.2.1 Time-varying loading solutions

The expression

$$\begin{aligned} \Delta\theta(x_1, x_2, x_3, t) \\ = \frac{1}{4\rho C(\pi D)^{3/2}} \int_{\tau=0}^t S(\tau) \frac{e^{-\frac{R^2}{4D(t-\tau)}}}{(t-\tau)^{3/2}} d\tau, \end{aligned} \quad (19)$$

which can be integrated numerically in the time-domain to produce the solution to time-varying heat input.

2.2.2 Spatially-varying loading solutions

Spatially-varying solutions can be constructed by superposing multiple ($i = 1, 2, \dots, N$) point loads (Fig. 1) within a

pattern (and hence R , one can generate the response for an entire patterned response

$$\Delta\theta^{tot-N}(x_1, x_2, x_3, t) = \sum_{i=1}^N \Delta\theta_i(x_1, x_2, x_3, t) \quad (20)$$

where

$$\Delta\theta_i(x_1, x_2, x_3, t) = \frac{1}{4\rho C(\pi D)^{3/2}} \int_{\tau=0}^t S_i(\mathbf{x}_i^*, t) \frac{e^{-\frac{R_i^2}{4D(t-\tau)}}}{(t-\tau)^{3/2}} d\tau, \quad (21)$$

which can be integrated numerically in the time-domain. In the limit, this becomes

$$\Delta\theta^{tot}(x_1, x_2, x_3, t) = \int_{\Omega} \Delta\theta_i(x_1, x_2, x_3, t) d\Omega, \quad (22)$$

where $S_i(\mathbf{x}_i^*, t)$ is replaced with $\delta S(\mathbf{x}, t)\delta\Omega$, $\delta S(\mathbf{x}, t)$ being Watts per unit volume. Numerically, the total thermal field at a point in the target is computed by summing all point load contributions ($i = 1, 2, \dots, N$, appropriately translated according to their position on the surface). The computational algorithm is as follows:

- INITIALIZATION: GENERATE A STARTING CONFIGURATION FOR THE LOADS
- STEP 1: COMPUTE THE HEAT N LOADING SITES.
- STEP 2: COMPUTE THE THERMAL FIELD CONTRIBUTION FROM EACH LOAD, $i = 1, 2, \dots, N$, ON THE SURFACE: $\Delta\theta_i(x_1, x_2, x_3, t)$,
- STEP 3: SUM THE CONTRIBUTIONS OF EACH LOAD, $i = 1, 2, \dots, N$, TO COMPUTE THE TOTAL: $\Delta\theta^{tot-N}(x_1, x_2, x_3, t)$,

$$\theta^{tot-N}(x_1, x_2, x_3, t) = \theta(t=0) + \Delta\theta^{tot-N}(x_1, x_2, x_3, t) \quad (23)$$

- STEP 4: REPEAT STEPS 1–3 FOR EACH TIME STEP.
- STEP 5: COMPUTE THE TARGET RESPONSE STATISTICS IN THE TARGET ZONE OF INTEREST AS DESIRED.

Figure 4 provides a corresponding flow chart for the process. It is important to note the quasi-stochastic nature of a laser beam is captured since at every time-step the heat kernel source terms are redistributing (fluctuating), as they would be in reality.

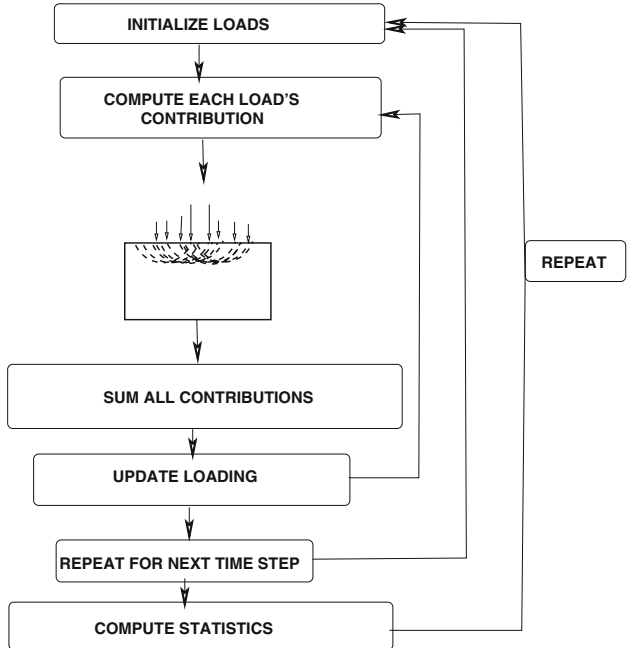


Fig. 4 The algorithm for computation of the loading of a surface

2.3 Thermal nonuniformity compensation-for any pattern

The utility of the approach is that one can ascertain detailed spatial distribution of the temperature field in the target. One can also post-process aggregate thermal field. For example, one *important* statistical metric is the standard deviation of the thermal field from the volume average temperature in the feature at any given moment in time:

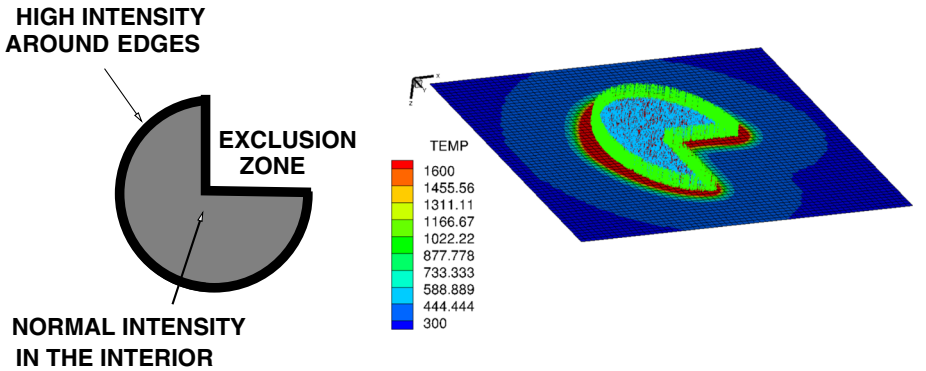
$$\alpha = \frac{\sqrt{\frac{1}{V_f} \int_{\Omega_f} (\theta^{tot-N}(\mathbf{x}) - \theta^{av})^2 d\mathbf{x}}}{\theta^{av}}, \quad (24)$$

where Ω_f is the domain of the feature, V_f is the volume of the feature and θ^{av} is the average temperature in the feature. One can foresee that from Eq. 13, repeated again below

$$\Delta\theta(x_1, x_2, x_3, t) = \frac{S}{4\rho C(\pi D)^{3/2}} \int_{\tau=0}^t \frac{e^{-\frac{R^2}{4D(t-\tau)}}}{(t-\tau)^{3/2}} d\tau, \quad (25)$$

that the temperature rise will be highest at the center of the feature and decreasing exponentially to the edge of the feature. Thus, we need to increase the intensity of the beam at the edges. The most practical way to do this is to identify the edges of the feature, and to increase the intensity of the beam in an “edge-zone”, Ω^e , which is a user-set standoff distance, creating a self-similar smaller pattern, as shown in Fig. 5. Mathematically, this can be expressed as

Fig. 5 Increased intensity applied to the edges to compensate for the heat decay



- If $x \in \Omega^e$, then $\hat{S}(x) = \hat{S}^e(x) > \hat{S}^i(x)$, where $\hat{S}^e(x)$ is the heating intensity per unit area in the edge zone and \hat{S}^i is the heating intensity in the interior.
- If $x \in \Omega^i$, then $\hat{S}(x) = \hat{S}^i(x) < \hat{S}^e(x)$, where Ω^i is the interior of the feature.
- The sum of the two areal contributions must be the total wattage applied ($S^{tot}(x)$) to the target area of the feature $\Omega^{tot} = \Omega^e + \Omega^i$:

$$\begin{aligned} \text{Total Wattage} &= S^{tot} = \int_{\Omega^{tot}} \hat{S}(x) d\Omega \\ &= \int_{\Omega^e} \hat{S}^e(x) d\Omega \\ &\quad + \int_{\Omega^i} \hat{S}^i(x) d\Omega. \end{aligned} \quad (26)$$

A relatively simple approach is to set:

$$\hat{S}^e = S^i \times A, \quad (27)$$

where $A > 1$ is an amplification over the interior intensity.

Remark One could also induce a gradual spatio-temporal beam adaptation:

$$\hat{S}^e(t) = S^i \times \left(1 + (A - 1) \frac{t}{T}\right) \quad (28)$$

where T is the total simulation time. We note that using t (a variable) would allow for adaptation in time as well.

2.4 Evolution of thermal stresses

We now illustrate how the results track the evolution of the thermal gradients and thermal softening and correlates that to the magnitude of the thermal stresses, using materials values previously introduced. As the results show, eventually the thermal gradients become nearly zero in the feature, and have high values at the feature-surrounding solid interface. To obtain more detailed information on the

complex phase transformations, a complete coupled thermo-mechanical formulation is presented, based on the papers of Zohdi located here: <http://cmmrl.berkeley.edu/77-2/>. The thermal-mechanical (residual) stress, σ , is given by the classical Hookean equation

$$\sigma = \mathbf{IE} : (\boldsymbol{\epsilon} - \boldsymbol{\epsilon}_\theta), \quad (29)$$

where \mathbf{IE} is the elasticity tensor, $\boldsymbol{\epsilon}$ is the total strain and $\boldsymbol{\epsilon}_\theta$ is the thermal strain given by

$$\boldsymbol{\epsilon}_\theta = \alpha(\theta(t) - \theta_o)\mathbf{1} \quad (30)$$

where α is the thermal expansion coefficient. In the isotropic case

$$\sigma = \mathbf{IE} : (\boldsymbol{\epsilon} - \boldsymbol{\epsilon}_\theta) = 3\kappa \frac{tr(\boldsymbol{\epsilon} - \boldsymbol{\epsilon}_\theta)}{3} \mathbf{1} + 2\mu \boldsymbol{\epsilon}', \quad (31)$$

where κ is the bulk modulus, μ is the shear modulus, $\frac{tr(\boldsymbol{\epsilon} - \boldsymbol{\epsilon}_\theta)}{3} \mathbf{1}$ is the dilatational strain, $\boldsymbol{\epsilon}'$ is the deviatoric strain. In a heated state the bulk modulus behaves approximately as ($\theta_o \leq \theta(t) \leq \theta_m$, a gradual change of phase)

$$\kappa(\theta(t)) = \kappa_s e^{-A \frac{\theta(t) - \theta_o}{\theta_o}} \quad (32)$$

where $A = -\frac{\theta_o}{\theta_m - \theta_o} \ln(\frac{\kappa_m}{\kappa_s})$, so that $\kappa(\theta_o) = \kappa_s$ (cool solid) and $\kappa(\theta_m) = \kappa_m$ (melted solid), with a cap placed on $\theta(t)$ in the constitutive law

$$\theta^{max}(t) = \theta_m. \quad (33)$$

Because this is a thermally-driven problem, the magnitude of the (residual) stress is approximately proportional to the magnitude of the thermal gradient at a point x

$$||\boldsymbol{\sigma}(\theta)|| \approx 3\kappa(\theta)\alpha ||\hat{\nabla}\theta|| \quad (34)$$

where $\hat{\nabla}\theta = \nabla\theta \cdot \Delta\mathbf{x}$, where $\Delta\mathbf{x}$ is the grid-spacing in the simulation between neighboring points ($\mathbf{x} \pm \Delta\mathbf{x}$) surrounding \mathbf{x} .

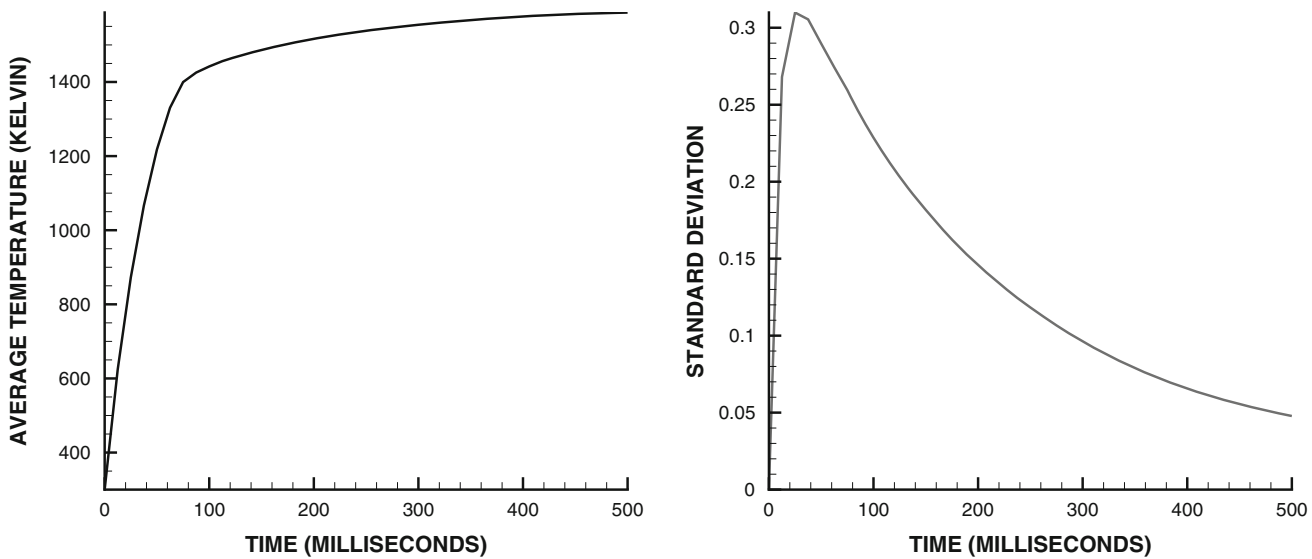


Fig. 6 UNIFORM BEAM: 25000 W laser/Stainless Steel. LEFT: The average temperature in the feature RIGHT: The standard deviation (α , Eq. 24) from the average temperature in the feature (500 ms)

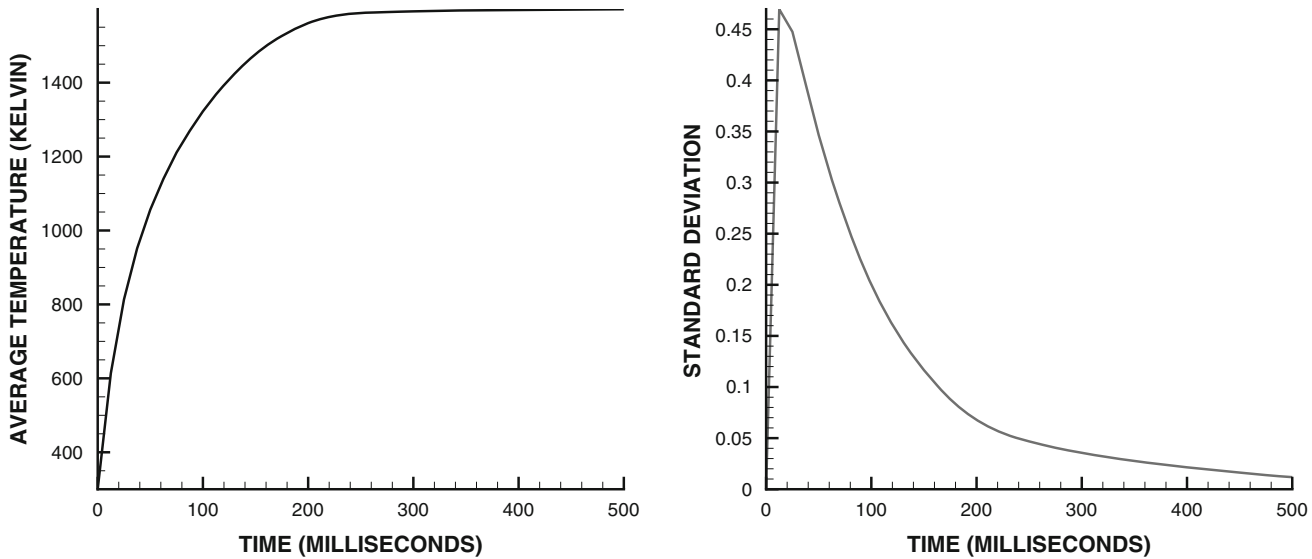


Fig. 7 NONUNIFORM BEAM: 25000 W laser/Stainless Steel. LEFT: The average temperature in the feature RIGHT: The standard deviation (α , Eq. 24) from the average temperature in the feature (500 ms)

2.5 Numerical studies

In order to illustrate the uniform vs. nonuniform beam concept, we compare the results of a uniform and nonuniform (edge-compensated) beam of 25000 W on the 3/4-circle domain (Fig. 5). The beam has been increased by a factor of five in the edge zone. The following specific laser and geometry following parameters were used:

- Starting temperature: $\theta(t = 0, \mathbf{x}) = 300 \text{ K}$,
- Laser power: 25000 W focused on the target dimensions,
- Elliptical disk dimensions: major axis = 0.015 m, minor axis = 0.01 m with one quadrant excluded (Fig. 5),

The following material parameter sets were used, for Stainless Steel:

- $\mathbf{IK} = 20 \text{ W/m-K}$,
- $\rho = 8000 \text{ kg/m}^3$,
- $C = 500 \text{ J/K-kg}$,
- $\theta_{melt} = 1600 \text{ K}$,
- $\kappa_s = 160 \text{ GPa}$, $\kappa_m \approx 0 \text{ GPa}$,
- $\alpha = 0.000015 \text{ m/K}$,

A sampling grid of $60(x) \times 60(y) \times 5(z)$ with 2000 randomly-distributed point-load heat kernels were used to generate the following (Figs. 6, 7, 8, 9, 10, 11, 12, 13, 14 and 15):

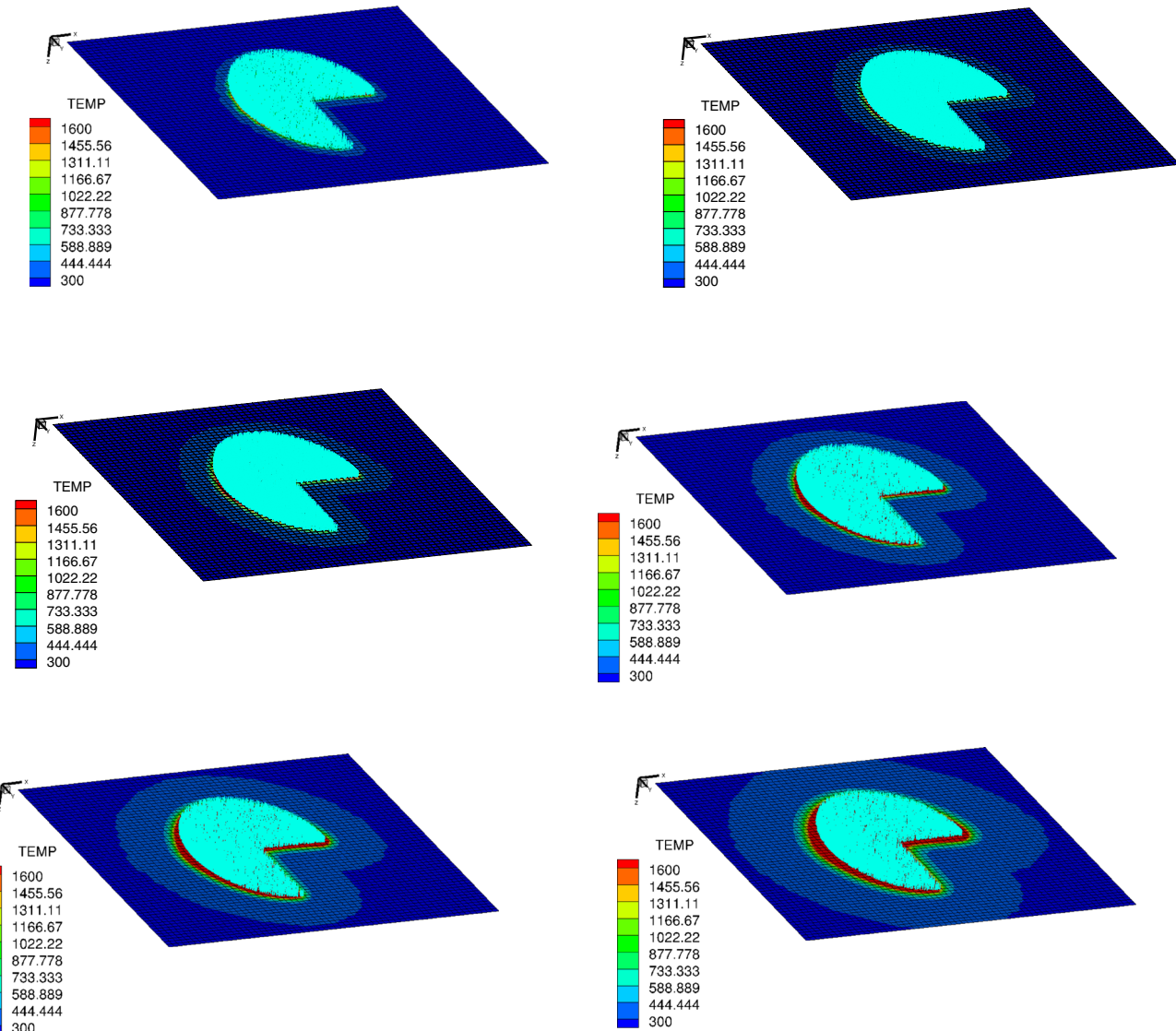


Fig. 8 UNIFORM BEAM: 25000 W laser/Stainless Steel (left to right and top to bottom). Sequence of thermal frames, viewed from above (500 ms)

- UNIFORM BEAM: 25000 W laser/Stainless Steel uniform laser. Averages and standard deviation (α , Eq. 24) from the average temperature in the feature.
- NONUNIFORM BEAM: 25000 W laser/Stainless Steel uniform laser. Averages and standard deviation (α , Eq. 24) from the average temperature in the feature.
- UNIFORM BEAM: 25000 W laser/Stainless Steel uniform laser. Sequence of the thermal fields $\theta(\mathbf{x})$.
- NONUNIFORM BEAM: 25000 W laser/Stainless Steel uniform laser. Sequence of the thermal fields $\theta(\mathbf{x})$.
- UNIFORM BEAM: 25000 W laser/Stainless Steel uniform laser. Sequence of the thermal stresses $||\boldsymbol{\sigma}||$.
- NONUNIFORM BEAM: 25000 W laser/Stainless Steel uniform laser. Sequence of the thermal stresses $||\boldsymbol{\sigma}||$.

2.6 Interpretation of the results

As the sequences show, eventually the thermal gradients become nearly zero in the feature, and have high values at the feature-surrounding interface. The code completes this entire process in under a minute on a Mac Powerbook, making it ideal for laser-system design studies. Figures 6 and 7 show the average temperature in the feature, as well as the standard deviation from the average. The thermal response to the nonuniform beam rises more slowly, relative to the uniform beam case and has a high standard deviation. For both beam types, the temperature eventually becomes homogeneous and the standard deviation drops. Figures 8, 9, 10, 11, 12, 13 and 15 depict these results more graphically, viewed

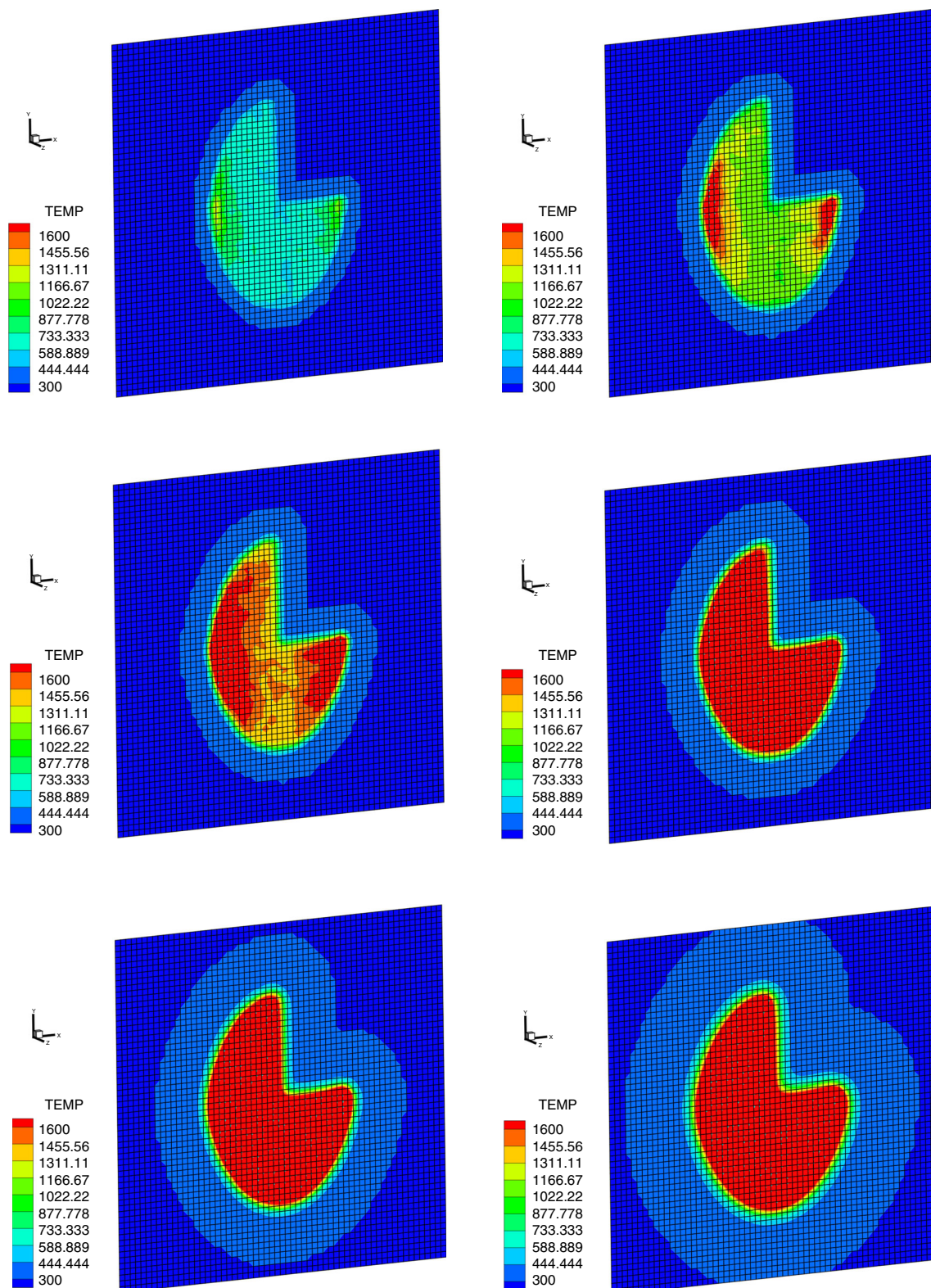


Fig. 9 UNIFORM BEAM: 25000 W laser/Stainless Steel(left to right and top to bottom). Sequence of thermal frames viewed from below (500 ms)

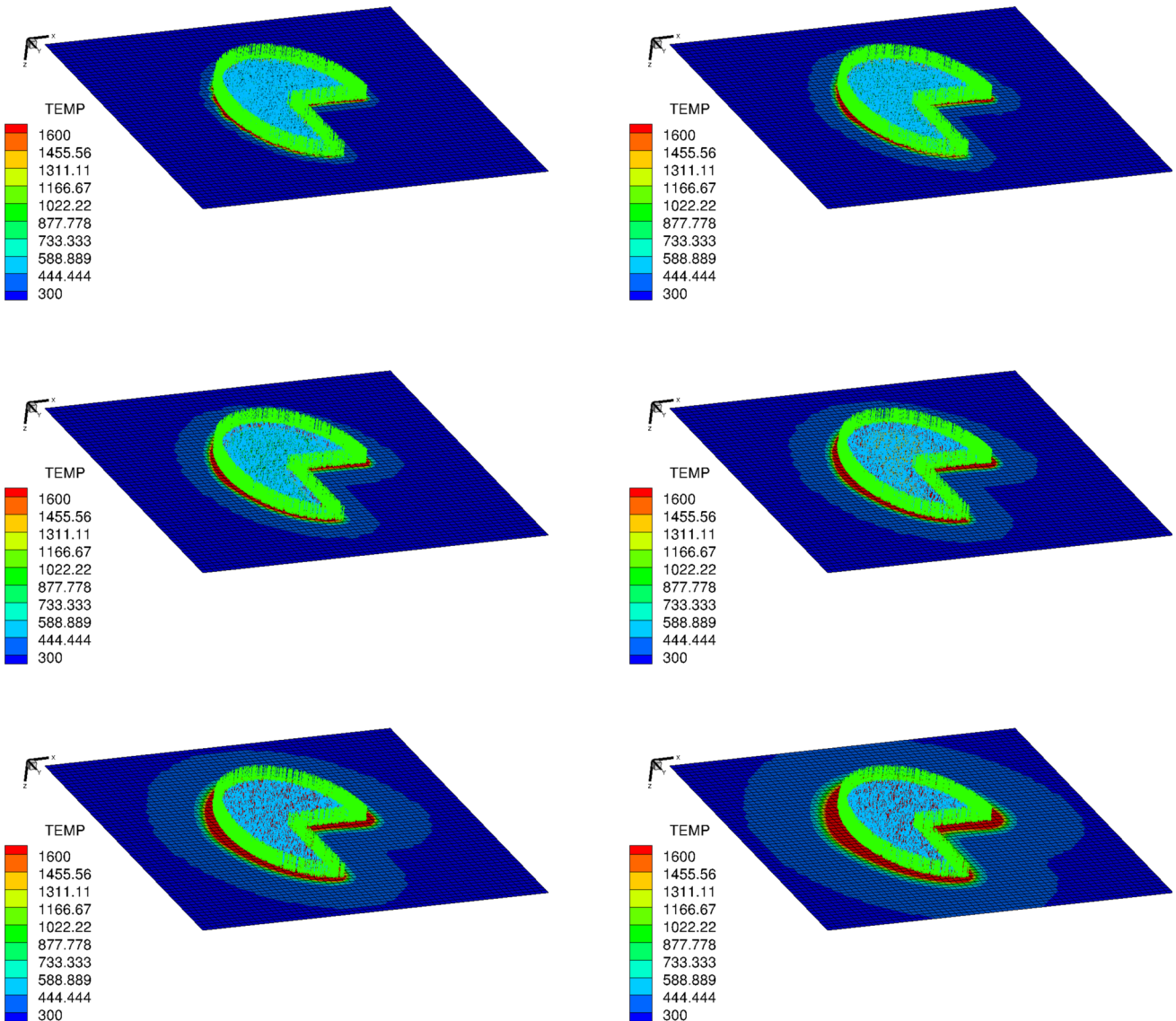


Fig. 10 NONUNIFORM BEAM: 25000 W laser/Stainless Steel (left to right and top to bottom). Sequence of thermal frames viewed from above (500 ms)

from above the feature and below. The “mesh” of sampling points is superposed to give an idea of the density of locations where the heat kernels have been summed in Eqs. 20–22. It is important to note the quasi-stochastic nature of a laser beam is captured since at every time-step the heat kernel source terms are redistributing (fluctuating), as they would be in reality.

3 Summary and extensions

In summary, the utility of the approach is that an analyst can efficiently ascertain a large number of laser-input scenarios without resorting to computationally-intensive numerical discretization procedures, such as the Finite Element Method.

Essentially, the method computes the thermal fields by superposing individual “beamlet” heat-kernel solutions, based on time-transient Green’s functions, to construct the overall thermal solutions due to complex surface patterns. This enables laser-processing designers to efficiently compute the resulting thermal system response of selecting various system parameters, such as spatially-variable laser intensity within a pattern. This allows one to rapidly compute system parameter studies needed in the manufacturing of new products. The presented analysis constructs a computational framework to compute the time-transient thermal response from a spatio-temporally non-uniform laser beam in an arbitrary spatial pattern and illustrates how the results can be used to track the evolution of the thermal gradients and their correlation to thermal stresses. Ultimately, analyst can effi-

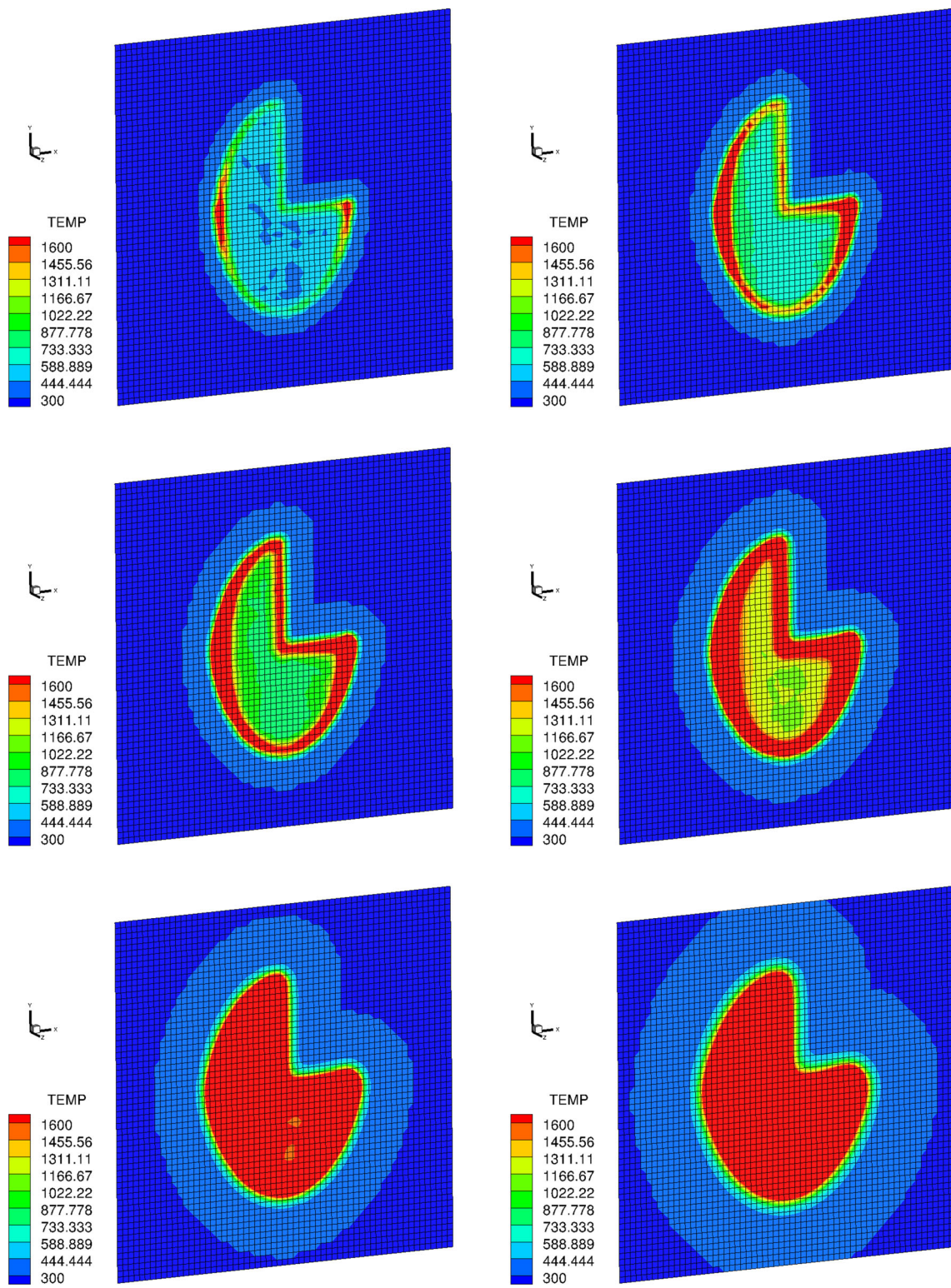


Fig. 11 NONUNIFORM BEAM: 25000 W laser/Stainless Steel(left to right and top to bottom). Sequence of thermal frames viewed from below (500 ms)

ciently ascertain the results of large number of laser-input scenarios, leaving more detailed, computationally-intensive, coupled thermo-mechanical PDE discretization of finite

sized domains, based on Finite Element or Finite Difference methods, for final analyses at the end of a system design phase.

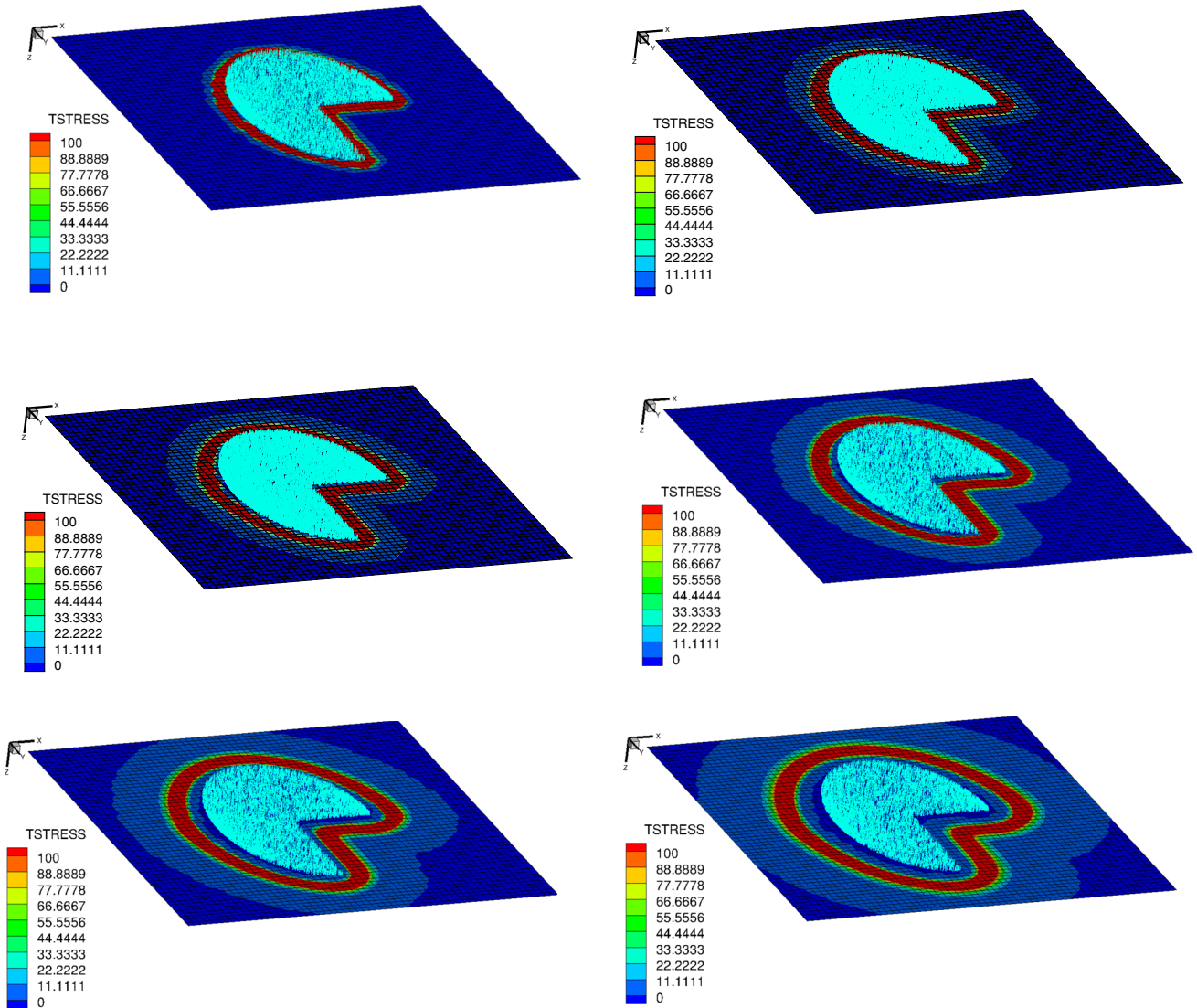


Fig. 12 UNIFORM BEAM: 25000 W laser/Stainless Steel uniform laser. Sequence of the thermal stresses $\|\sigma\|$ viewed from above (500 ms)

As a practical matter, the use of this method is to test several hundred, if not thousand, laser-processing scenarios as a system parameter optimization tool. At the end of a system design phase, in order to obtain more rigorous values of the thermally-induced stress fields, phase-transformations, melting, resolidification and even ablation, etc., one will have to solve a computationally-intensive coupled thermo-mechanical initial boundary value problem with phase transformations, consisting of solving a balance of linear momentum governed by

$$\nabla_x \cdot \boldsymbol{\sigma} + \mathbf{f} = \rho \frac{d^2 \mathbf{u}}{dt^2}, \quad (35)$$

and the interconversions of various forms of energy (mechanical, thermal, etc) in a system are governed by the first law of thermodynamics,

$$\rho \dot{w} - \boldsymbol{\sigma} : \nabla_x \dot{\mathbf{u}} + \nabla_x \cdot \mathbf{q} - \rho z = 0, \quad (36)$$

where w is the stored energy per unit mass, which is a function of the temperature (θ) and deformation gradient $\nabla \mathbf{u}$, \mathbf{q} is heat flux, and $\rho z = S^{vol}$ is the rate of energy absorbed from sources (laser). Following a series of works in Zohdi [34–46], a laser-penetration model, in conjunction with a Finite Element or Finite Difference Time Domain (FDTD) Method using an immersed microstructure method. To include phase transformations, one must consider seven cases, which were implemented in a predictor-corrector manner by first solving the governing equations to obtain predicted temperature, and then checking the following:

- *Solid \rightarrow solid-no melting with $C_i = C_S$:* If $\theta(t) < \theta_m$ and $\theta(t + \Delta t) < \theta_m$ then retain $C(\theta) = C_S$,
- *Solid \rightarrow liquid-melting with $C_i = C_S$:* If $\theta(t) < \theta_m$ and $\theta(t + \Delta t) \geq \theta_m$ then re-solve the governing equations with $C(\theta) = C_S + \frac{\delta \mathcal{P}^{S \rightarrow L}}{\delta \theta}$,

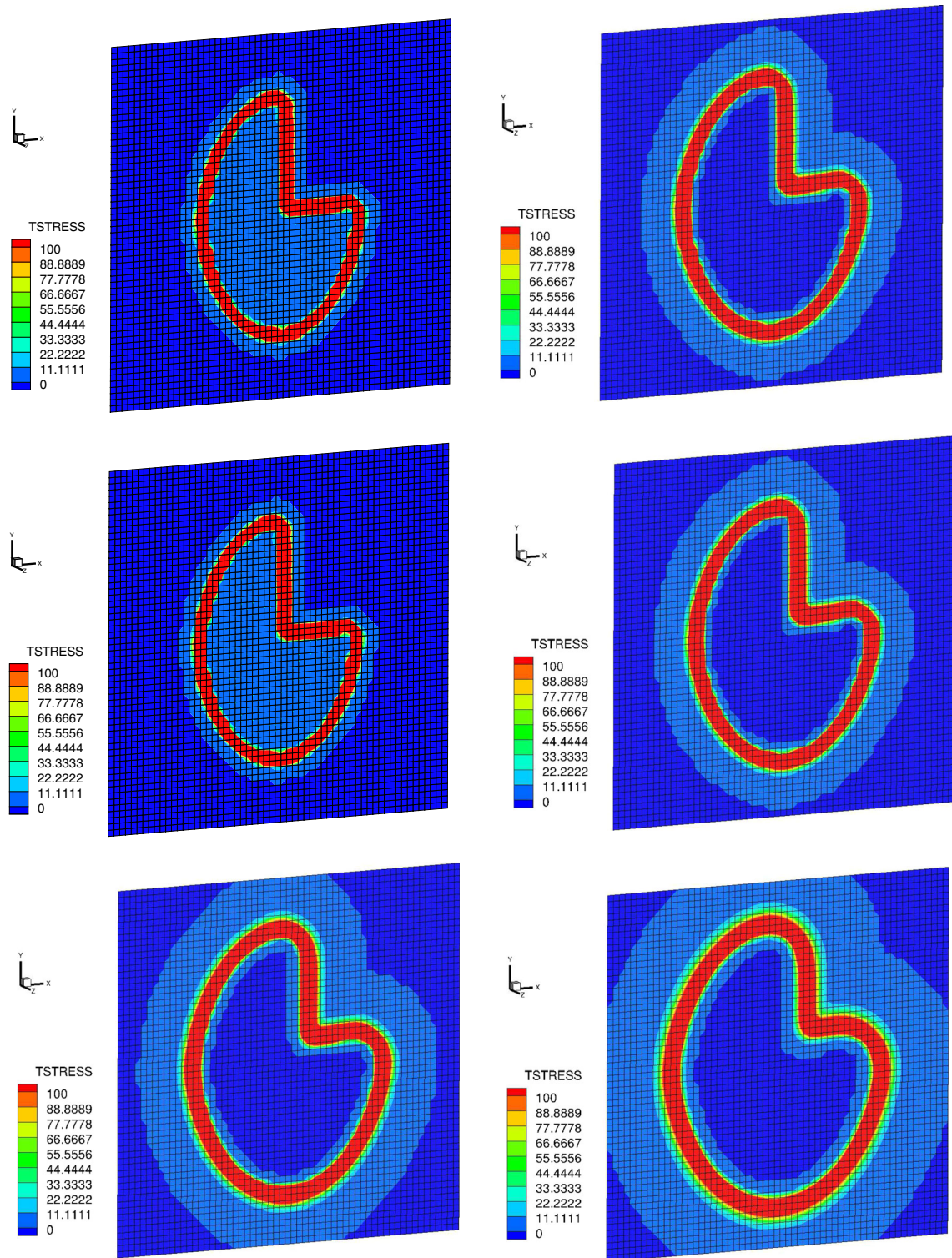


Fig. 13 UNIFORM BEAM: 25000 W laser/Stainless Steel uniform laser. Sequence of the thermal stresses $||\sigma||$ viewed from below (500 ms)

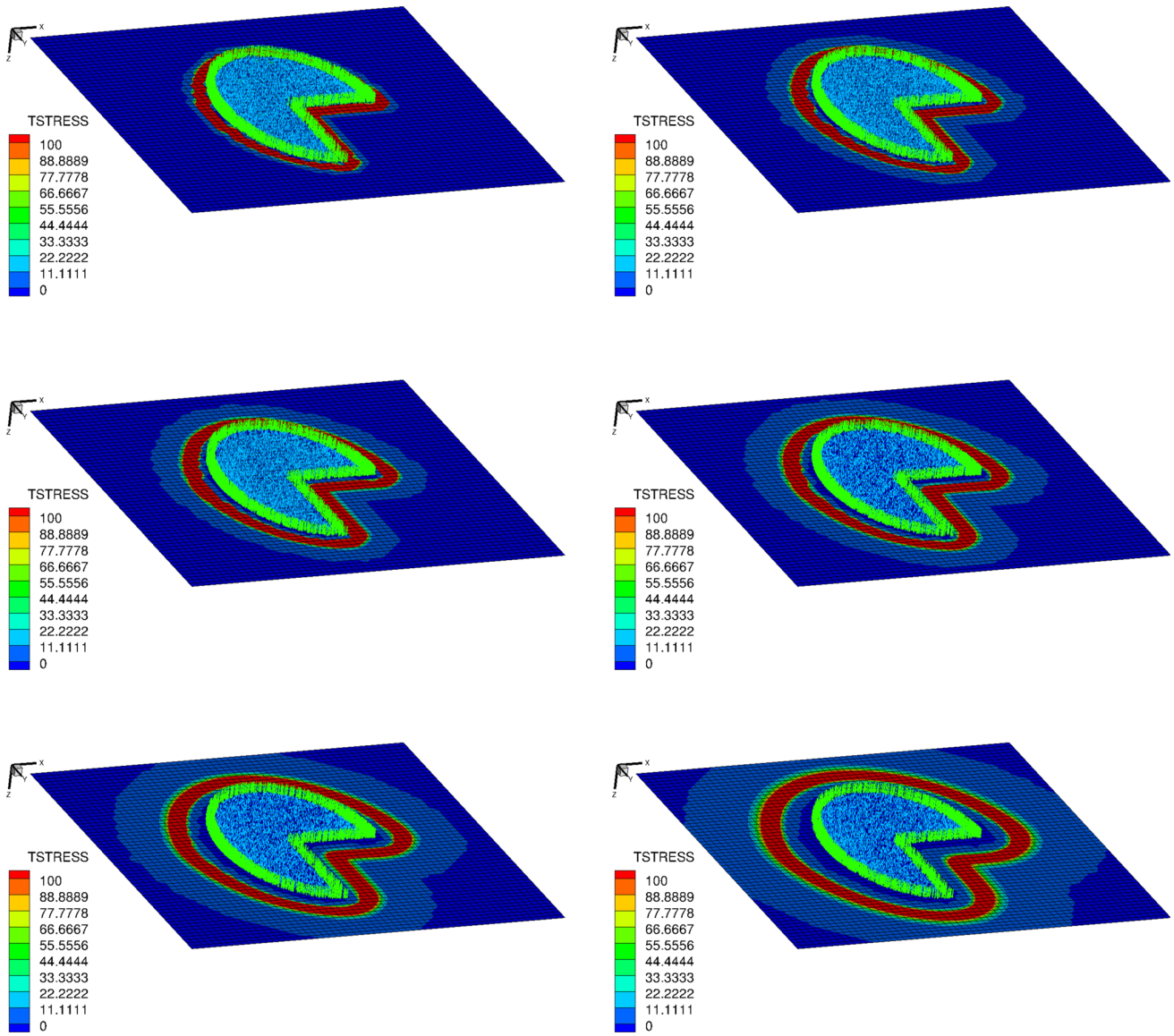


Fig. 14 NONUNIFORM BEAM: 25000 W laser/Stainless Steel uniform laser. Sequence of the thermal stresses $||\sigma||$ viewed from above (500 ms)

- *Liquid \rightarrow liquid-melted with $C_i = C_L$:* If $\theta(t) \geq \theta_m$ and $\theta(t + \Delta t) \geq \theta_m$ then retain $C(\theta) = C_L$,
- *Liquid \rightarrow solid-solidification with $C_i = C_L$:* If $\theta(t) \geq \theta_m$ and $\theta(t + \Delta t) < \theta_m$ then re-solve the governing equations with $C(\theta) = C_L + \frac{\delta\mathcal{P}^{L \rightarrow S}}{\delta\theta}$,
- *Liquid \rightarrow vapor-vaporization with $C_i = C_L$:* If $\theta(t) < \theta_v$ and $\theta(t + \Delta t) \geq \theta_v$ then re-solve governing equations with $C(\theta) = C_L + \frac{\delta\mathcal{P}^{L \rightarrow V}}{\delta\theta}$,
- *Vapor \rightarrow vapor-remains a vapor with $C_i = C_V$:* If $\theta(t) \geq \theta_v$ and $\theta(t + \Delta t) \geq \theta_v$ then retain $C(\theta) = C_V$,
- *Vapor \rightarrow liquid-condensation with $C_i = C_v$:* If $\theta(t) \geq \theta_v$ and $\theta(t + \Delta t) < \theta_v$ then re-solve the governing equations with $C(\theta) = C_V + \frac{\delta\mathcal{P}^{V \rightarrow L}}{\delta\theta}$,

where C_S is the heat capacity of the solid, C_L is the heat capacity of the liquid and C_V is the heat capacity of the vapor and and

- $0 < \delta\mathcal{P}^{S \rightarrow L}$ is the latent heat of melting,
- $0 < \delta\mathcal{P}^{L \rightarrow S}$ is the latent heat of solidification,
- $0 < \delta\mathcal{P}^{L \rightarrow V}$ is the latent heat of vaporization,
- $0 < \delta\mathcal{P}^{V \rightarrow L}$ is the latent heat of condensation and
- $0 < \delta\theta$ is small and can be thought of as a “bandwidth” for a phase transformation. For more details on melting processes, see Davis [7].

We note that latent heats have a tendency to resist the phase transformations, achieved by adding the positive terms in

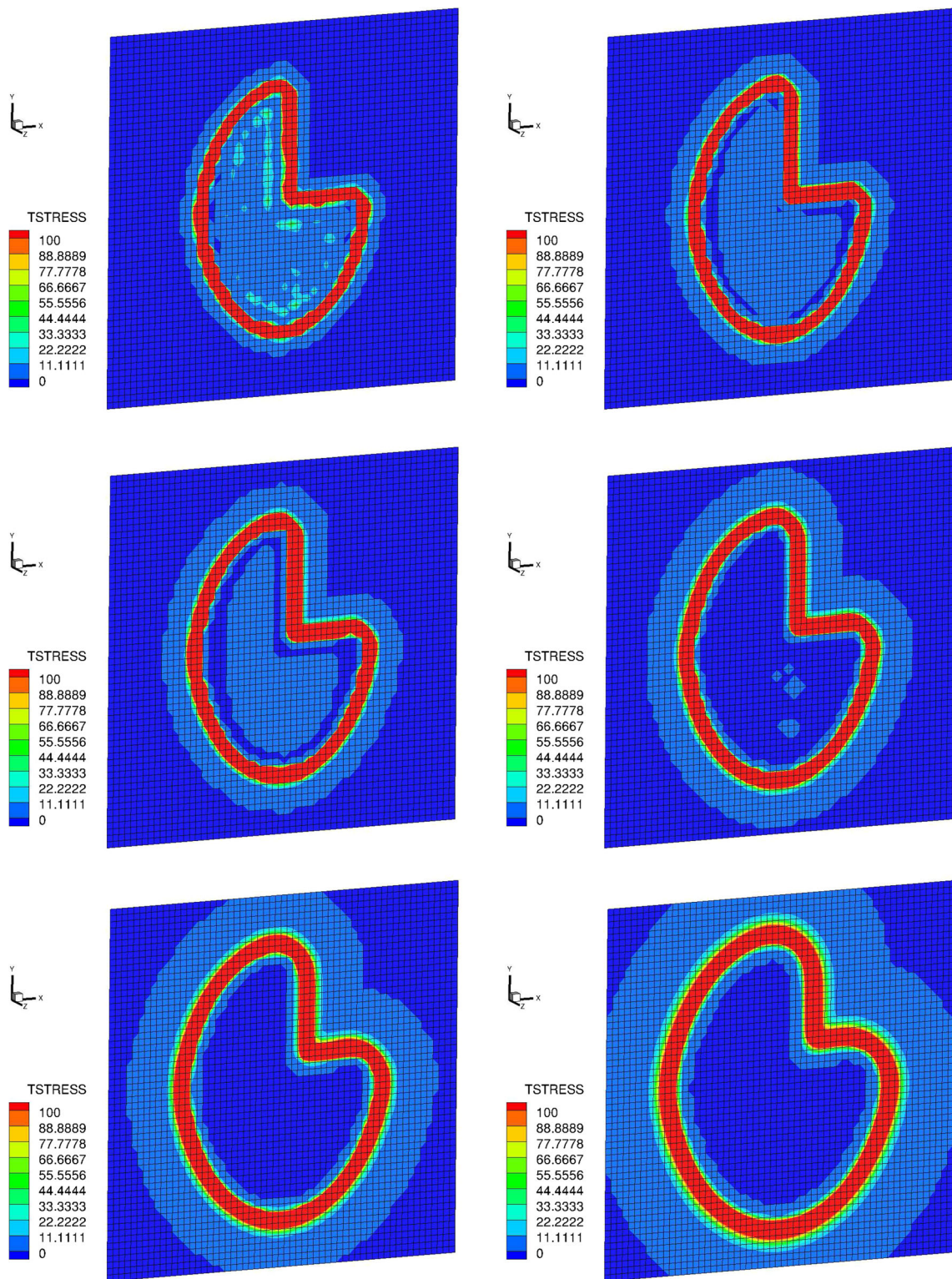


Fig. 15 NONUNIFORM BEAM: 25000 W laser/Stainless Steel uniform laser. Sequence of the thermal stresses $\|\sigma\|$ viewed from below (500 ms)

the denominator, thus enforcing reduced temperature (during the phase transformation).³ This approach is relatively

straightforward to include within the staggering framework. Because strong thermal and mechanical (and possibly optical) multifield coupling is present, a recursive, staggered, temporally-adaptive scheme was developed to resolve the

³ In the idealized limit, the temperature would be constant.

internal microstructural fields. The time step adaptation allows the numerical scheme to iteratively resolve the changing physical fields by refining the time-steps during phases of the process when the system is undergoing large changes on a relatively small time-scale and can also enlarge the time-steps when the processes are relatively slow. Following Zohdi [34–46], a staggering solution framework was developed to solve the coupled systems of interest. The general methodology is as follows (at a given time increment): (1) each field equation is solved individually, “freezing” the other (coupled) fields in the system, allowing only the primary field to be active and (2) after the solution of each field equation, the primary field variable is updated, and the next field equation is treated in a similar manner. For an “implicit” type of staggering, the process can be repeated in an iterative manner, while for an “explicit” type, one moves to the next time step after one “pass” through the system. For example one could employ implicit staggering. Specifically, for the thermo-mechanical system under consideration, consider an abstract setting, whereby one solves for the mechanical field, assuming the thermal field is fixed (L is a time-step counter and K is a staggering-step counter),

$$\mathcal{A}_1(\underline{\mathbf{u}^{L+1,K}}, \underline{\theta^{L+1,K-1}}) = \mathcal{B}_1(\mathbf{u}^{L+1,K-1}, \theta^{L+1,K-1}) \quad (37)$$

then one solves for the thermal fields, assuming the mechanical field fixed,

$$\mathcal{A}_2(\mathbf{u}^{L+1,K}, \underline{\theta^{L+1,K}}) = \mathcal{B}_2(\mathbf{u}^{L+1,K}, \theta^{L+1,K-1}) \quad (38)$$

where the only underlined variable is “active” at that stage of the process. Within the staggering (iterative) scheme, implicit time-stepping methods are used, with time step size adaptivity. The adaptive process is driven by minimizing nondimensional relative iterative coupling error (of both fields) within a time-step (difference between successive iterations). A tolerance check determines whether the iterations should continue, or if the time steps should be adaptively reduced to increase the rate of convergence. The time steps can be increased if convergence occurs too quickly, thus allowing larger time-steps and faster simulations for a given iterative error tolerance. Generally speaking, if a recursive staggering process is not employed (an explicit coupling scheme), the staggering error can accumulate rapidly. However, simply employing extremely small time steps, smaller than needed to control the discretization error, in order to suppress a (nonrecursive) staggering process error, can be computationally inefficient. Therefore, a strategy was developed to adaptively adjust, in fact maximize, the choice of the time step size in order to control the staggering error, while simultaneously staying below a critical time step size

needed to control the discretization error. An important related issue is to simultaneously minimize the computational effort involved. See Zohdi [34–46] and papers posted here <http://cmmrl.berkeley.edu/77-2/>.

Acknowledgements The author acknowledges generous support from Siemens Grant 85702-23845-44-EKZOH-EEZT85702X, under program manager Dr. Marco Brunelli.

References

1. Ahmad Z, Rasekh M, Edirisinha M (2010) Electrohydrodynamic direct writing of biomedical polymers and composites. *Macromol Mater Eng* 295:315–319
2. Carslaw HS, Jaeger JC (1959) Conduction of heat in solids, 2nd edn. Clarendon Press, Oxford
3. Choi S, Park I, Hao Z, Holman HY, Pisano AP, Zohdi TI (2010) Ultra-fast self-assembly of micro-scale particles by open channel flow. *Langmuir* 26(7):4661–4667
4. Choi S, Stassi S, Pisano AP, Zohdi TI (2010) Coffee-ring effect-based three dimensional patterning of micro, nanoparticle assembly with a single droplet. *Langmuir* 26(14):11690–11698
5. Choi S, Jamshidi A, Seok TJ, Zohdi TI, Wu MC, Pisano AP (2012) Fast, High-throughput creation of size-tunable micro, nanoparticle clusters via evaporative self-assembly in picoliter-scale droplets of particle suspension. *Langmuir* 28(6):3102–11
6. Choi S, Pisano AP, Zohdi TI (2013) An analysis of evaporative self-assembly of micro particles in printed picoliter suspension droplets. *J Thin Solid Films* 537(30):180–189
7. Davis SH (2001) Theory of solidification. Cambridge University Press, Cambridge
8. Demko M, Choi S, Zohdi TI, Pisano AP (2012) High resolution patterning of nanoparticles by evaporative self-assembly enabled by in-situ creation and mechanical lift-off of a polymer template. *Appl Phys Lett* 99:253102-1–253102-3
9. Demko MT, Cheng JC, Pisano AP (2010) High-resolution direct patterning of gold nanoparticles by the microfluidic molding process. *Langmuir* 26:412–417
10. Dwivedi G, Wentz T, Sampath S, Nakamura T (2010) Assessing process and coating reliability through monitoring of process and design relevant coating properties. *J Therm Spray Technol* 19:695–712
11. Fathi S, Dickens P, Khodabakhshi K, Gilbert M (2013) Microcrystalline particles behaviour in inkjet printing of reactive nylon materials. *J Manuf Sci Eng* 135:011009. <https://doi.org/10.1115/1.4023272>
12. Fuller SB, Wilhelm EJ, Jacobson JM (2002) Ink-jet printed nanoparticle microelectromechanical systems. *J Microelectromech Syst* 11:54–60
13. Gamota D, Brazis P, Kalyanasundaram K, Zhang J (2004) Printed organic and molecular electronics. Kluwer Academic Publishers, New York
14. Grekov MA, Kostyrko SA (2015) A multilayer film coating with slightly curved boundary. *Int J Eng Sci* 89:61–74
15. Huang D, Liao F, Molesa S, Redinger D, Subramanian V (2003) Plastic-compatible low-resistance printable gold nanoparticle conductors for flexible electronics. *J Electrochem Soc* 150(7):G412–417
16. Huang Y, Leu MC, Mazumdar J, Donmez A (2015) Additive manufacturing: current state, future potential, gaps and needs, and recommendation. *J Manuf Sci Eng* 137:014001–1
17. Jaeger JC (1942) Moving sources of heat and the temperature of sliding contacts. *Proc R Soc NSW* 76:203–224

18. Kachanov M, Shafiro B, Tsukrov I (2003) Handbook of elasticity solutions. Kluwer, New York
19. Kennedy FE (2001) Frictional heating and contact temperatures. In: The modern tribology handbook. CRC Press
20. Liu Y, Nakamura T, Dwivedi G, Valarezo A, Sampath S (2008) Anelastic behavior of plasma sprayed zirconia coatings. *J Am Ceram Soc* 91:4036–4043
21. Liu Y, Nakamura T, Srinivasan V, Vaidya A, Gouldstone A, Sampath S (2007) Nonlinear elastic properties of plasma sprayed zirconia coatings and associated relationships to processing conditions. *Acta Mater* 55:4667–4678
22. Martin P (2009) Handbook of deposition technologies for films and coatings, 3rd edn. Elsevier, Amsterdam
23. Martin P (2011) Introduction to surface engineering and functionally engineered materials. Scrivener and Elsevier. *J Vac Sci Technol A* 2(2):500
24. Nakanishi H, Bishop KJM, Kowalczyk B, Nitzan A, Weiss EA, Tretiakov KV, Apodaca MM, Klajn R, Stoddart JF, Grzybowski BA (2009) Photoconductance and inverse photoconductance in thin films of functionalized metal nanoparticles. *Nature* 460:371–375
25. Nakamura T, Liu Y (2007) Determination of nonlinear properties of thermal sprayed ceramic coatings via inverse analysis. *Int J Solids Struct* 44:1990–2009
26. Nakamura T, Qian G, Berndt CC (2000) Effects of pores on mechanical properties of plasma sprayed ceramic coatings. *J Am Ceram Soc* 83:578–584
27. Qian G, Nakamura T, Berndt CC (1998) Effects of thermal gradient and residual stresses on thermal barrier coating fracture. *Mech Mater* 27:91–110
28. Samarasinghe SR, Pastoriza-Santos I, Edirisinghe MJ, Reece MJ, Liz-Marzan LM (2006) Printing gold nanoparticles with an electrohydrodynamic direct write device. *Gold Bull* 39:48–53
29. Sevostianov I, Kachanov M (2000) Modeling of the anisotropic elastic properties of plasma-sprayed coatings in relation to their microstructure. *Acta Mater* 48(6):1361–1370
30. Sevostianov I, Kachanov M (2001) Thermal conductivity of plasma sprayed coatings in relation to their microstructure. *J Therm Spray Technol* 9(4):478–482
31. Sevostianov I, Kachanov M (2001) Plasma-sprayed ceramic coatings: anisotropic elastic and conductive properties in relation to the microstructure. cross-property correlations. *Mater Sci Eng A* 297:235–243
32. Sirringhaus H, Kawase T, Friend RH, Shimoda T, Inbasekaran M, Wu W, Woo EP (2000) High-resolution inkjet printing of all-polymer transistor circuits. *Science* 290:2123–2126
33. Wang JZ, Zheng ZH, Li HW, Huck WTS, Sirringhaus H (2004) Dewetting of conducting polymer inkjet droplets on patterned surfaces. *Nat Mater* 3:171–176
34. Zohdi TI (2002) An adaptive-recursive staggering strategy for simulating multifield coupled processes in microheterogeneous solids. *Int J Numer Methods Eng* 53:1511–1532
35. Zohdi TI (2004) Modeling and simulation of a class of coupled thermo-chemo-mechanical processes in multiphase solids. *Comput Methods Appl Mech Eng* 193(6–8):679–699
36. Zohdi TI (2007) Computation of strongly coupled multifield interaction in particle-fluid systems. *Comput Methods Appl Mech Eng* 196:3927–3950
37. Zohdi TI (2008) On the computation of the coupled thermo-electromagnetic response of continua with particulate microstructure. *Int J Numer Methods Eng* 76:1250–1279
38. Zohdi TI (2010) Simulation of coupled microscale multiphysical-fields in particulate-doped dielectrics with staggered adaptive FDTD. *Comput Methods Appl Mech Eng* 199:79–101
39. Zohdi TI (2013) Rapid simulation of laser processing of discrete particulate materials. *Arch Comput Methods Eng*. <https://doi.org/10.1007/s11831-013-9092-6>
40. Zohdi TI (2014) A computational modeling framework for heat transfer processes in laser-induced dermal tissue removal. *Comput Mech Eng Sci* 98(3):261–277
41. Zohdi TI (2014) Additive particle deposition and selective laser processing-a computational manufacturing framework. *Comput Mech* 54:171–191
42. Zohdi T.I. (2015) Rapid computation of statistically-stable particle/feature ratios for consistent substrate stresses in printed flexible electronics. *J Manuf Sci Eng ASME. MANU-14-1476* <https://doi.org/10.1115/1.4029327>
43. Zohdi TI (2015) Modeling and simulation of cooling-induced residual stresses in heated particulate mixture depositions. *Comput Mech* 56:613–630
44. Zohdi TI (2015) Modeling and simulation of laser processing of particulate-functionalized materials. *Arch Comput Methods Eng*. <https://doi.org/10.1007/s11831-015-9160-1>
45. Zohdi TI, Wriggers P, (2005, 2008) Introduction to computational micromechanics. Second Reprinting. Springer-Verlag
46. Zohdi, T. I. (2012) Electromagnetic properties of multiphase dielectrics. A primer on modeling, theory and computation. Springer-Verlag